Nano Energy 102 (2022) 107743

Contents lists available at ScienceDirect

Nano Energy

journal homepage: www.elsevier.com/locate/nanoen

Ferro-pyro-phototronic effect enhanced self-powered, flexible and ultra-stable photodetectors based on highly crystalized 1D/3D ferroelectric perovskite film

Zheng Yang [a,b,1], Xiaoli Li [a,1], Linjie Gao [a], Wei Zhang [a], Xinzhan Wang [a], Haixu Liu [a], Shufang Wang [a,*], Caofeng Pan [b,*], Linjuan Guo [a,*]

[a] Hebei Key Laboratory of Optic-Electronic Information and Materials, National & Local Joint Engineering Laboratory of New Energy Photoelectric Devices, College of Physics Science and Technology, Hebei University, Baoding 071002, PR China
[b] CAS Center for Excellence in Nanoscience, Beijing Institute of Nanoenergy and Nanosystems, Chinese Academy of Sciences, Beijing 100083, PR China

ARTICLE INFO

Keywords:
Ferro-pyro-phototronic effect
Self-powered photodetector
1D/3D perovskite
Flexible devices
Interface modulation

ABSTRACT

Self-powered and flexible perovskite photodetectors are holding great promise owing to their potential for high-performance wearable and portable optoelectronic applications. The light-induced ferro-pyro-phototronic effect can boost the performances of ferroelectric materials-based photodetector systems significantly. However, the utilization of the ferro-pyro-phototronic effect in polycrystalline halide perovskites films-based flexible photodetectors is rarely mentioned. Here, a ferro-pyro-phototronic effect boosted self-powered, flexible, and ultra-stable photodetector based on 1D/3D mixed perovskite ferroelectric film/P3HT heterojunction is demonstrated. By employing $Pb(SCN)_2$ as lead source to partially for fabricating high-quality $MAPbI_3$ film and incorporating 1D ferroelectric perovskite $TMIMPbI_3$, the overall optoelectronic performances were largely enhanced, with a low dark current of 7×10^{-9} A, a responsivity of 6.6 mA/W and a detectivity of 5×10^9 Jones. The PDs displayed good folding endurance, and anti-humidity stability. The excellent performance is attributed to the reduced trap-density and enhanced pyro-phototronic effect induced by improved crystallinity and introduced ferroelectricity.

1. Introduction

Recently, metal halide perovskites have attracted much attention for their various optoelectronic applications, such as solar cells, light-emitting diodes and photodetectors (PDs), since they have excellent characteristics such as large light absorption coefficient, high carrier mobility, and low trap density [1–4]. However, most of the reported perovskite PDs are fabricated on rigid substrates, which are not compatible with wearable or flexible systems. Another issue that limits the practical application of existing PDs is that they usually require an external power source to separate the photogenerated carriers, which increases the device cost and weight. One class of the common approaches to realize self-powered photodetection is construction of p-i-n, p-n or Schottky junctions [5,6]. Those heterojunction-based self-powered PDs' performances depend highly on the built-in electric field formed at the heterojunction interface [7]. Therefore, these self-powered PDs can be further boosted by combining other physical mechanisms such as the ferroelectric effect [8,9] and the pyro-phototronic effect [10,11], which can remarkably enhance the built-in electric field.

Recently, the light-induced ferro-pyro-phototronic effect of ferroelectrics has been utilized to significantly improve the ITO/$BaTiO_3$/Ag Schottky junction [12], $BaTiO_3$/GaN heterojunction [13], and two-dimensional perovskite single crystal [14]-based PDs' performances. The light-generated heating or cooling will increase or decrease the ferroelectric polarization charges at the interface, which can effectively modulate the photoelectric process of light-induced carriers. Therefore, the overall photoelectric performances are significantly enhanced, and self-powered photodetection can also be realized. Ferroelectric halide perovskites, which combine excellent optoelectronic performance, spontaneous polarization, and natural pyroelectric properties [15,16], are an ideal platform to fabricate

* Corresponding authors.
E-mail addresses: sfwang@hbu.edu.cn (S. Wang), cfpan@binn.cas.cn (C. Pan), guolinjuan@hbu.edu.cn (L. Guo).
[1] Zheng Yang and Xiaoli Li contributed equally to this work.

https://doi.org/10.1016/j.nanoen.2022.107743
Received 5 May 2022; Received in revised form 20 July 2022; Accepted 21 August 2022
Available online 25 August 2022

ferro-pyro-phototronic effect based self-powered PDs. In our previous work, by using the ferro-pyro-phototronic effect, a self-powered PMA_2PbCl_4 monocrystalline microbelt-based PD with high photo-responsivity and fast responses is demonstrated [17]. However, the utilization of the ferro-pyro-phototronic effect in polycrystalline halide perovskites films to enhance the performance of flexible photodetectors is rarely mentioned. Recently, by incorporating 1D ferroelectric $TMIMPbI_3$ [$(CH_3)_3NCH_2IPbI_3$] with 3D hybrid perovskites ($FAPbI_3$), the overall performances of the solar cells are enhanced due to the reduced surface recombination induced by ferroelectricity [18]. Therefore, further research is needed to prepare 1D/3D ferroelectric perovskite films for fabricating high performance and self-powered photodetector.

Besides, the crystallinity and orientation of grains in perovskites films are crucial to optoelectronic and polar performances [19,20]. Chao et al. reported a dense, pinhole-free, and high-quality perovskite film using room-temperature molten salt, methylammonium acetate (MAAc), as solvent [21]. However, the low-boiling point of MAAc induced rapid crystallization process will result in smaller grain size and more grain boundaries. Wang et al. demonstrated a non-halide engineering, which simultaneously employed $Pb(AC)_2$ and $Pb(SCN)_2$ as lead sources for fabricating high-quality $MAPbI_3$ films in ambient air [22]. Therefore, using room-temperature molten salt as the solvent and non-halide salt $Pb(SCN)_2$ to partially replace PbI_2, high-quality $MAPbI_3$ films with large grain, higher crystallinity, and preferential orientation will be obtained.

Herein, a self-powered, flexible, and ultra-stable photodetector based on 1D /3D mixed perovskite ferroelectric film/P3HT heterojunction boosted by ferro-pyro-phototronic effect is demonstrated. First, high-quality $MAPbI_3$ films with large grain size and consistent orientation were obtained by a one-step hot spin-coating method using MAAc as the solvent and partially replacing PbI_2 with $Pb(SCN)_2$. Further, 1D room temperature ferroelectric perovskite $TMIMPbI_3$ was incorporated into $MAPbI_3$ film to form 1D/3D mixed perovskite film. With an optimized ratio of $Pb(SCN)_2/PbI_2$ and incorporation of 1D ferroelectric perovskite, the overall photo-sensing performances were largely enhanced, with a responsivity of 6.6 mA/W, which is improved by over 2.5 times, compared with the PbI_2-based film. This enhancement should attribute to the reduced carrier recombination and enhanced pyro-phototronic effect induced by better crystallinity and introduced ferroelectricity. Furthermore, the PDs display good folding endurance and anti-humidity stability. The unencapsulated PD retains 82% of initial pyroelectric response and undergoes no photocurrent decay after being stored in 80 ± 10% humidity for 39 days. Our work will provide a new route of utilizing the ferro-pyro-phototronic effect to efficiently enhance the performance of perovskite films-based PDs and other optoelectronic devices.

2. Results and discussion

$MAPbI_3$ films with different $PbI_2/Pb(SCN)_2$ molar ratios (1:0, 0:1, 1:1, 3:1, 7:1 and 9:1) in precursor solution were prepared by one-step hot spin-coating process at 90 °C under ambient conditions [25 °C, 30

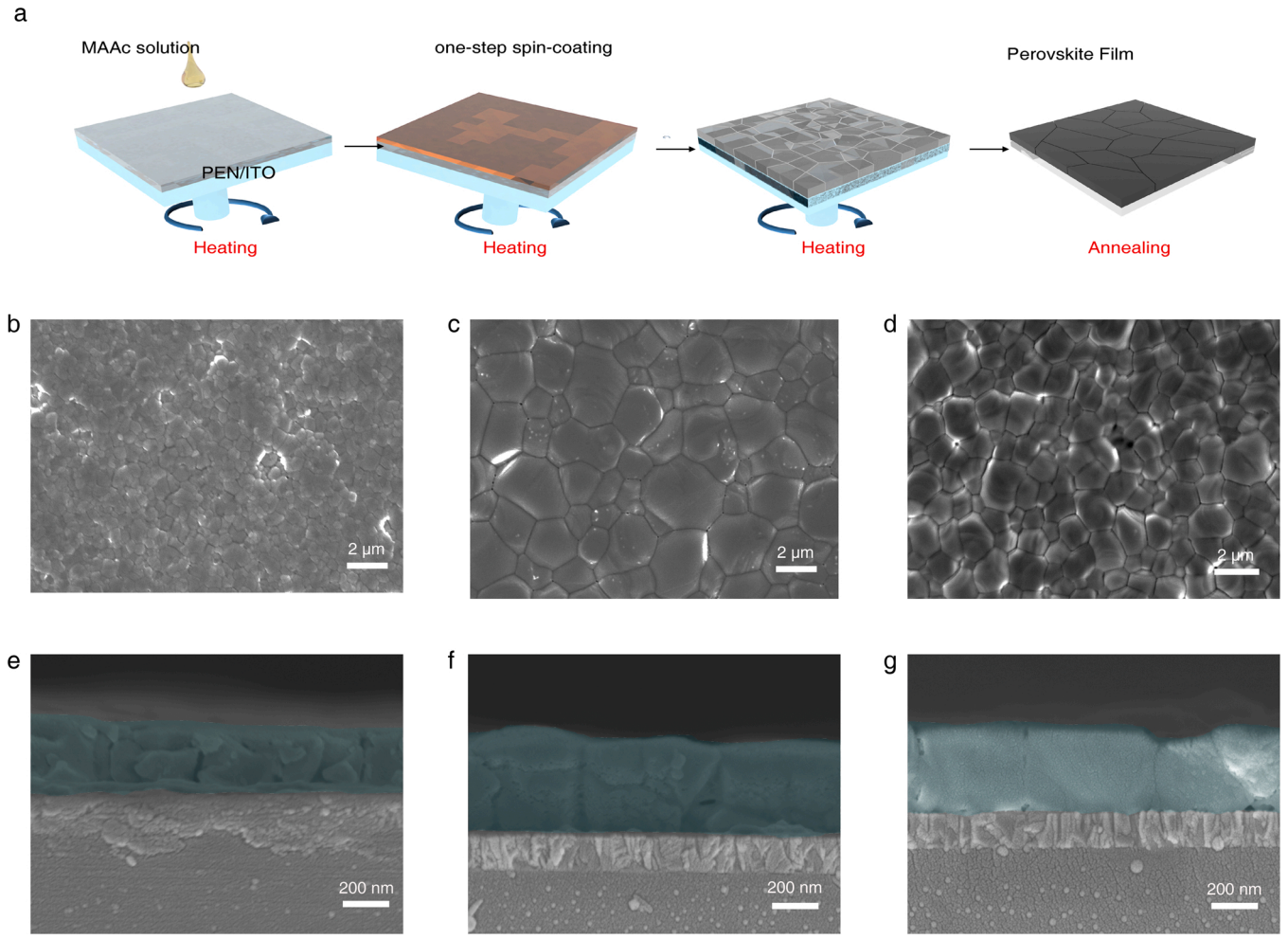

Fig. 1. (a) Schematic illustration of the fabrication procedures of perovskite film. (b-d) The top view and (e-g) cross-sectional view SEM images of the PbI_2, $PbI_2/Pb(SCN)_2$, and $PbI_2/Pb(SCN)_2$-TMIMI perovskite films on ITO substrates.

± 10% relative humidity (RH)]. 1, 3-Diaminopropane (DAP) was added to the solution to enhance the resistance of films to mechanical bending, according to the reference [23]. The brief preparation procedures are schematically shown in Fig. 1a. The content of $Pb(SCN)_2$ has a significant influence on the morphology of the final perovskite films. From the scanning electron microscope (SEM) image in Fig. 1b, the PbI_2-based perovskite film ($PbI_2/Pb(SCN)_2$ molar ratio = 1:0) was dense and uniform, with relatively small grain size (average grain size of 590 nm). After the replacement of SCN^-, although films with much larger grains were obtained, however, the poor coverage with many micron-scale pores was observed, especially when higher amounts of $Pb(SCN)_2$ were used. From Fig. S1, one can find that with the increase of the $PbI_2/Pb(SCN)_2$ molar ratio, both the number and size of pores gradually decrease. There still exist some pinholes in the film prepared with a $PbI_2/Pb(SCN)_2$ molar ratio of 7:1. Finally, homogeneous and pinhole-free perovskite film with an average grain size of 2.2 μm could be obtained with a $PbI_2/Pb(SCN)_2$ molar ratio of 9:1 (Fig. 1c). Afterward, the 1D/3D mixed perovskite film was fabricated using the above optimization condition except that 0.65 mol% (relative to Pb^{2+}, 3.6 mM) of TMIMI (Trimethyliodomethylammonium iodide) was added. Here, the concentration of 3.6 mM is close to the limiting concentration of TMIMI in MAAc. As shown in Fig. 1d, the 1D/3D mixed perovskite film also had a homogeneous and pinhole-free surface, without obvious change in the morphology except for a degree of grain size decrease (average grain size of 1.4 μm), which may be attributed to that TMIMI can induce a faster nucleation rate. The perovskite films made from pure PbI_2, $PbI_2/Pb(SCN)_2$ (molar ratio of 9:1), and $PbI_2/Pb(SCN)_2$ with TMIMI doping are defined as PbI_2 perovskite, $PbI_2/Pb(SCN)_2$ perovskite, and $PbI_2/Pb(SCN)_2$-TMIMI perovskite, respectively. Fig. 1e-g present the cross-sectional SEM images of the three perovskite films. The PbI_2 perovskite film was composed of small grains with a thickness of 300 nm, while the other two films ($PbI_2/Pb(SCN)_2$ perovskite and $PbI_2/Pb(SCN)_2$-TMIMI perovskite) exhibited identical monolithic grains from top to bottom, with the thickness of 500 nm and 470 nm, respectively.

As shown in Fig. 2a, the XRD patterns of PbI_2 perovskite film show two dominant diffraction peaks at 14.2° and 28.5°, corresponding to the (110) and (220) crystal planes of $MAPbI_3$, respectively, indicating that the perovskite films possess good crystal orientation and tetragonal structure. Besides, no peak at 12.7° which belongs to unreacted PbI_2 is found. When $Pb(SCN)_2$ was introduced, the intensities of the two dominant diffraction peaks increased, illustrating the enhanced crystallinity of the films. After the further doping of 1D perovskite, a small peak at $2\theta \approx 10°$ appeared in the $PbI_2/Pb(SCN)_2$-TMIMI perovskite film (inset of Fig. 2a), which can be attributed to the presence of 1D phase ($TMIMPbI_3$) in the 1D/3D mixed perovskite film [24]. The 1D/3D mixed

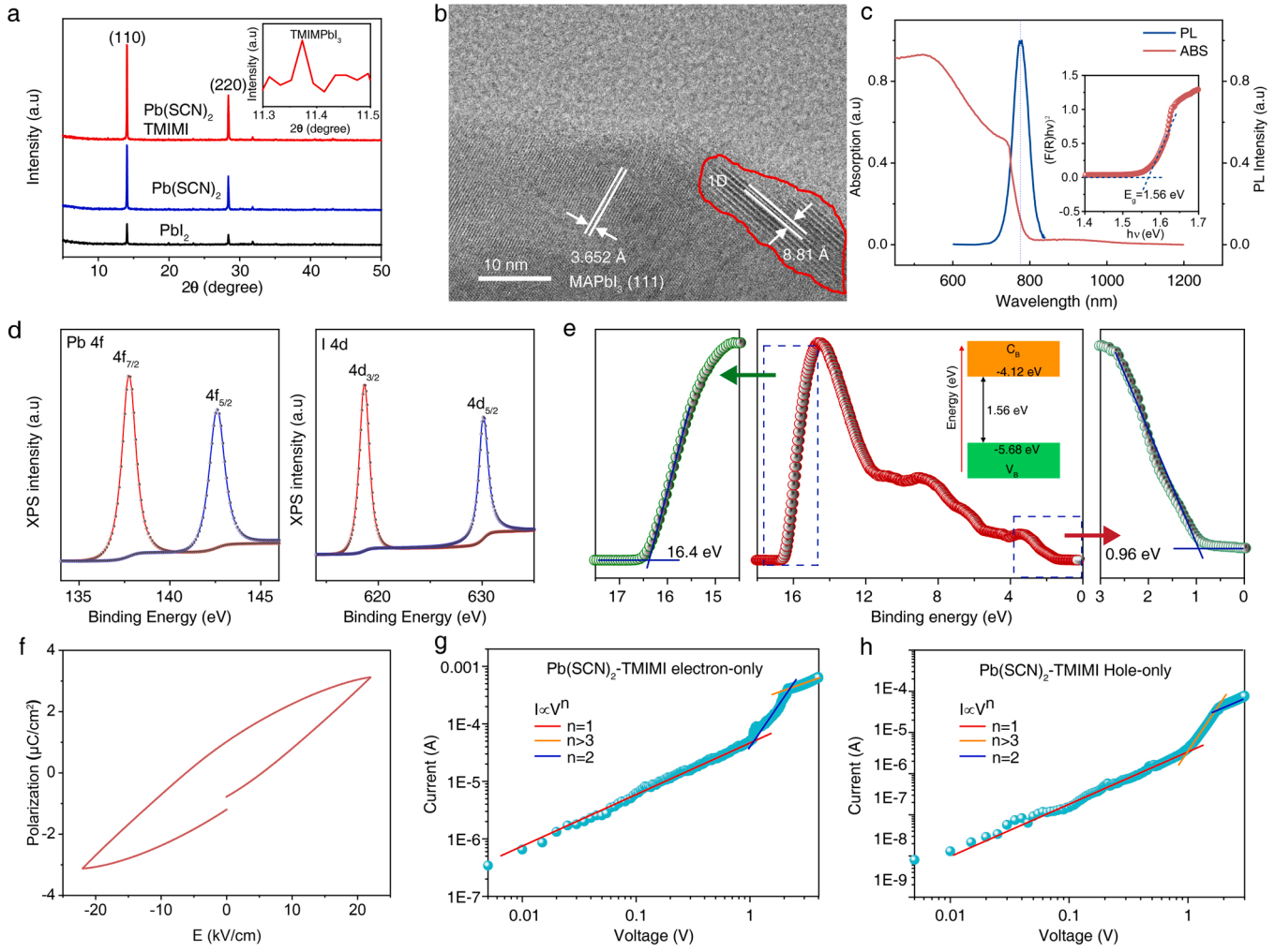

Fig. 2. (a) XRD patterns of the PbI_2, $PbI_2/Pb(SCN)_2$, and $PbI_2/Pb(SCN)_2$-TMIMI perovskite films. (b) HRTEM image of the $PbI_2/Pb(SCN)_2$-TMIMI perovskite film, showing the existence of 1D perovskite. (c) The absorbance spectrum and PL spectrum of the $PbI_2/Pb(SCN)_2$-TMIMI perovskite film. The inset is the corresponding Tauc plot, showing a bandgap of 1.56 eV. (d) XPS spectra of Pb 4f and I 4d for $PbI_2/Pb(SCN)_2$-TMIMI perovskite film. (e) UPS spectrum of the $PbI_2/Pb(SCN)_2$-TMIMI perovskite film. The inset is the corresponding energy band diagram. (f) *P-E* hysteresis loop, current-voltage curves of the (g) electron-only and (h) hole-only of the $PbI_2/Pb(SCN)_2$-TMIMI perovskite film.

perovskite can be formed since $TMIMPbI_3$ has a similar same PbI_6 octahedra backbone with $MAPbI_3$ [18,25]. To further investigate the incorporation of 1D perovskite into $MAPbI_3$ matrix, high-resolution transmission electron microscope (HRTEM) was performed. From Fig. 2b, one can see that the 1D $TMIMPbI_3$ can be identified from $MAPbI_3$ matrix according to the different diffraction plane. According to the literature [18], the XRD and HRTEM results, we can infer that by adding the TMIMI in the precursor solution, the 1D/3D mixed perovskite film can be formed since they possess the same PbI_6 octahedra framework. From Fig. S2, one can see that the PbI_2/$Pb(SCN)_2$-TMIMI perovskite film has small full width at half maximums (FWHMs) of 0.095° for (110) and 0.121° for (220), respectively. While for the PbI_2 perovskite film, the FWHMs are 0.116° and 0.0353°, respectively. The absorption and photoluminescence (PL) spectra of the three kinds of films are shown in Fig. S3. No apparent shifts are observed both for the absorption and PL spectra. As shown in Fig. S3a, the PbI_2 perovskite film had the lowest PL intensity. In contrast, the PbI_2/$Pb(SCN)_2$-TMIMI perovskite film exhibited the highest PL intensity, indicating that the PbI_2/$Pb(SCN)_2$-TMIMI perovskite film has the reduced non-radiative recombination loss and lower trap density. An absorption edge at 780 nm was observed in Fig. 2b, corresponding to a bandgap of 1.56 eV (inset of Fig. 2b), consistent with the reported $MAPbI_3$ films [21] made from the hot-casting method. The PL lifetimes of the three films were evaluated using time-resolved PL. As shown in Fig. S4, all the three decay curves behave a biexponential feature, with the shorter one representing the surface recombination and longer one representing the bulk recombination, respectively. The lifetime of the PbI_2/$Pb(SCN)_2$-TMIMI perovskite film representing the bulk recombination is the longest among the three perovskite films. once again proving the suppressed carrier recombination in the PbI_2/$Pb(SCN)_2$-TMIMI perovskite film. However, the lifetime of the PbI_2/$Pb(SCN)_2$-TMIMI perovskite film representing the surface is lowest, which may derive from the weakened surface with obvious wrinkles.

In addition, the chemical states of Pb and I in the PbI_2/$Pb(SCN)_2$-TMIMI perovskite film were determined using X-ray photoelectron spectroscopy (XPS) spectrum (Fig. 2d). The peaks of Pb 4 f (138.40 and 143.25 eV) and I 3d (630 and 618 eV) can be attributed to the Pb-I bonds in $MAPbI_3$ film. Peak rising from Pb^0 (uncoordinated Pb^{2+}) didn't appear, proving that no iodine vacancies exist [26]. From ultraviolet photoelectron spectroscopy (UPS) results in Fig. 2e, the valence band edge position and the Fermi level of the PbI_2/$Pb(SCN)_2$-TMIMI perovskite film were estimated, with the Fermi level and the valence band edge locating at − 4.72 eV and − 5.68 eV, respectively, relative to the vacuum level. Therefore, we can deduce that the conduction band locates at − 4.12 eV. Polarization-electric field (*P-E*) hysteresis loop of PbI_2/$Pb(SCN)_2$-TMIMI perovskite film in Fig. 2f behaves as obvious ferroelectric hysteresis that possesses both residual polarization and strong coercive field. In contract, no hysteresis phenomena for the other two perovskite films were observed (Fig. S5), proving the role of the 1D ferroelectric phase in 1D/3D mixed perovskite film. The trap densities of three perovskite films were determined by the space charge limited current (SCLC) method. Both hole-only devices (ITO/PEDOT:PSS (4083)/perovskite/TFB/Au) and electron-only devices (ITO/SnO_2/perovskite/PC61BM/Ag) were fabricated, and the dark current-voltage (*I-V*) curves of these devices were measured (Fig. 2g-h, Fig. S6). Trap densities can be calculated by the following equation:

$$n_{trap} = \frac{2\varepsilon_0 \varepsilon_r V_{TFL}}{eL^2} \quad (1)$$

where ε_0 is the vacuum permittivity, ε_r is the relative dielectric constant, V_{TFL} is the trap-filled limit voltage, e is the electron charge, and L is the film thickness. Here, ε_r of 32 is obtained from the literature [27], and V_{TFL} can be obtained from the dark *I-V* curves. Therefore, the hole-trap densities and electron-trap densities were calculated (Fig. S7). The lowest trap densities were determined for the PbI_2/$Pb(SCN)_2$-TMIMI based film, in accordance with the PL and TRPL characterizations. The reduced trap densities in the perovskite film indicate fewer defects, which may derive from reduced carrier recombination induced by ferroelectricity. Besides, the PbI_2/$Pb(SCN)_2$-TMIMI perovskite film reveals n-type conduction with n_{trap} of 2.77×10^{15} cm^{-3}, consistent with the UPS analysis.

Later, we fabricated p-n junction-based flexible PDs using 1D/3D mixed perovskite film as the n-type layer and P3HT as the p-type layer, with a device structure of PEN/ITO/perovskite/P3HT/Ni/Au. In the meantime, two control devices (PbI_2 perovskite and $Pb(SCN)_2$ perovskite) with the same device structure were also fabricated. Before spin-coating of P3HT, the perovskite films were successively cleaned, healed with MAI, and modified with tetra-ethyl ammonium iodide (TEAI). The detailed procedure is described in Experimental Section. The contact angles of water were tested on the PbI_2/$Pb(SCN)_2$-TMIMI perovskite film with and without TEAI (Fig. S8). The contact angle significantly increased from 56.3° to 106.9° after the modification of TEAI, indicating the hydrophobicity of the film, which could significantly improve the stability of the devices. The schematic structure of the self-powered and flexible PD is illustrated in Fig. 3a. From the cross-sectional SEM image of a typical PD in Fig. 3b, multiple layers with clear boundaries can be observed. Corresponding energy levels of each component in the PD are presented in Fig. 3c. The work function of PEIE treated ITO substrate (4.3 eV) was determined by UPS measurement (Fig. S9). The highest occupied molecular orbital (HOMO) and lowest unoccupied molecular orbital (LUMO) of P3HT are − 5.2 and − 3.2 eV, respectively [28]. The optical image of the PD is shown in Fig S10. To quantify the optoelectronic performances of PbI_2/$Pb(SCN)_2$-TMIMI perovskite-based PDs, the systematic photoresponses of the self-powered PD towards illumination were measured. First, we compared the overall performances of the three kinds of devices. Before testing, 1 V bias was applied to the devices for at least 1 min to obtain negative polarization. Fig. 3d and Fig. S11 show the *I-V* curves of the three PDs under 532 nm light illumination, all showing rectifying characteristics, indicating the formation of p-n heterojunction. Besides, the PbI_2/$Pb(SCN)_2$-TMIMI perovskite-based PD has the highest photocurrent while the PbI_2-based one has the lowest photocurrent. In addition, the PbI_2/$Pb(SCN)_2$-TMIMI perovskite-based PD has the lowest dark current at zero bias (Fig. S12). The suppressed dark currents may be attributed to the lower trap densities restrained by ferroelectricity. As shown in Fig. S13, the noise spectral density was estimated to be about 1.25×10^{-12} A $Hz^{-1/2}$ for PbI_2/$Pb(SCN)_2$-TMIMI perovskite-based PD, 2.81×10^{-12} A $Hz^{-1/2}$ for PbI_2/$Pb(SCN)_2$ perovskite-based PD, and 1.09×10^{-12} A $Hz^{-1/2}$ for PbI_2 perovskite-based PD at the bandwidth of 1 Hz, respectively, by performing a Fourier transform (FFT) of the dark current according to the reported literature [29]. Also, we can find that the noise current is dependent on the frequency, indicating that the noise of the present devices is dominated by the 1/f noise. What's more, the ferroelectricity of 1D/3D perovskite significantly enhances the built-in field to separate and transport the photogenerated carriers. The *I-V* curves of PbI_2/$Pb(SCN)_2$-TMIMI perovskite-based PD under 360, 450, and 785 nm laser illumination are measured and plotted in Fig. S14, respectively. Upon laser illuminations, all the curves show obvious photoresponse behavior both at 1 V forward bias and reverse bias. Fig. S15a and S15b show the *I-t* and *I-V* curves of the PD illuminated using the monochromatic laser with wavelengths ranging from 360 to 785 nm under the same power density (31.8 μW/cm^2), respectively, from which one can see that the PD shows the highest photocurrent towards 785 nm illumination. Besides, all the four *I-t* curves show obvious four-stage photo-response behaviors. For 532 nm, the relative peak-to-peak output current ($I_{pyro+photo}$-$I_{pyro'}$)/I_{photo} ratio is more signicant than that for 785 nm (Fig. S15c). The definition of $I_{pyro+photo}$-$I_{pyro'}$, $I_{pyro+photo}$, and I_{photo} will be given latter. Therefore, a 532 nm laser was used as the main light source. Fig. S16 shows the *I-t* curves of the three PDs under 532 nm light illumination, from which one can see that both the PbI_2/$Pb(SCN)_2$-TMIMI perovskite and PbI_2/$Pb(SCN)_2$ perovskite-based PDs show obvious pyroelectric

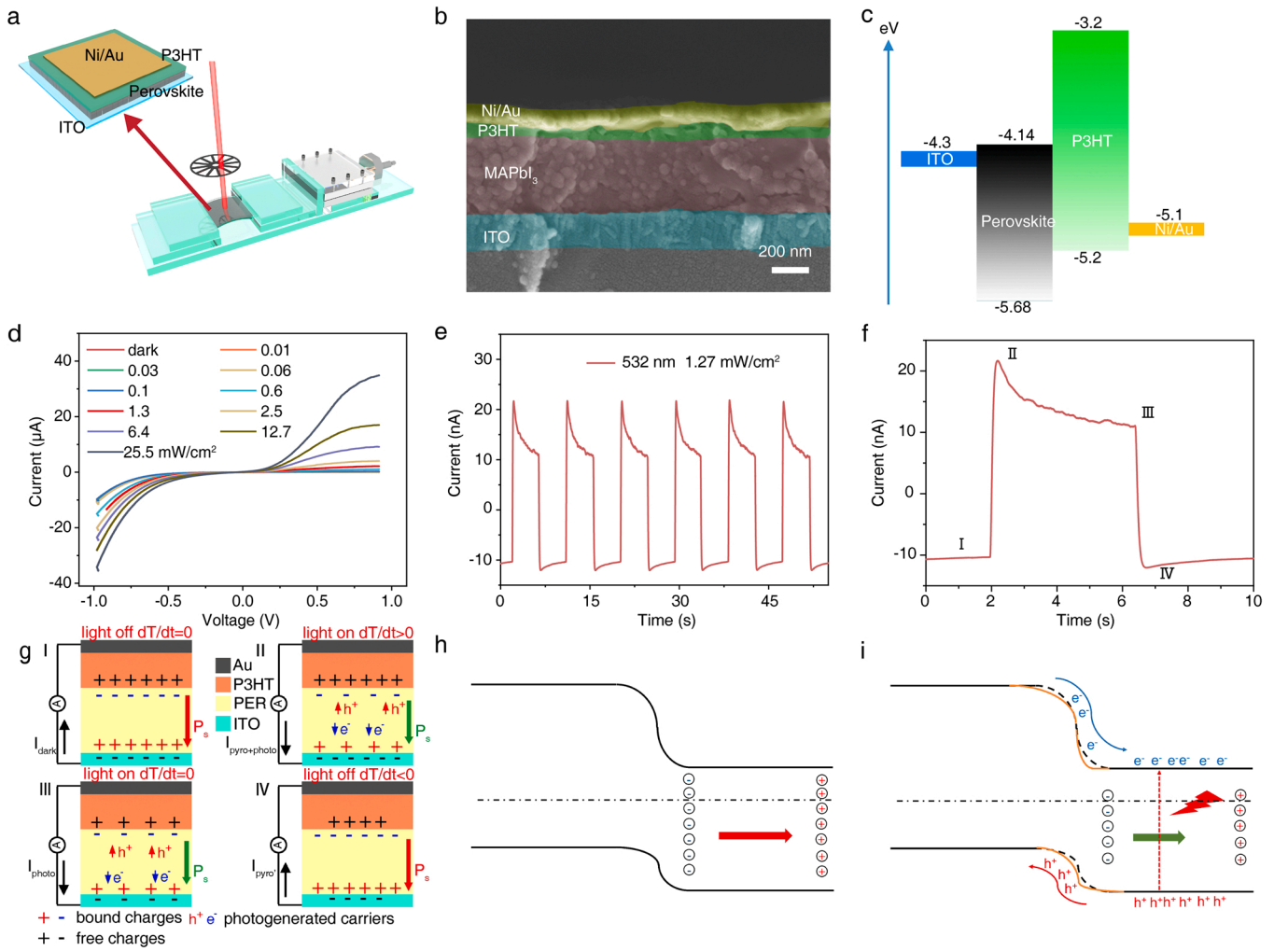

Fig. 3. (a) Schematic diagram of (left) the structure of the PD and (right) experimental setup to measure the photoresponses under bending conditions. (b) Cross-sectional SEM image of a typical PD fabricated in this study. (c) Energy band diagram of the PDs, using the electron energy in the vacuum as a reference. (d) *I-V* characteristics of the PbI_2/Pb(SCN)$_2$-TMIMI perovskite based PD under 532 nm illumination with different power densities ranging from 0 to 25.5 mW/cm^2. (e) Photoresponse behavior of the PbI_2/Pb(SCN)$_2$-TMIMI perovskite-based PD under 532 nm laser illumination with the power density of 0.13 mW/cm^2 under zero bias. (f) An enlarged view taken from Fig. 3e, displaying a typical four-stage photoresponse behavior. (g) Schematic working mechanism of the ferro-pyro-phototronic effect of the PD as turning on and turning off the laser. Energy band diagrams of the PDs under (h) dark and (i) light conditions.

current while the PbI_2 perovskite-based PD only shows photocurrent. Among the three PDs, the one based on the PbI_2/Pb(SCN)$_2$-TMIMI perovskite demonstrates the highest photo-response. Then *I-t* curves of the PbI_2/Pb(SCN)$_2$-TMIMI perovskite-based PD under repeated light on/off cycles towards 532 nm laser illumination (0.18 mW/cm^2) with zero bias are shown in Fig. 3e. An enlarged cycle of on-off response taken from Fig. 3e is presented in Fig. 3f. A four-stage photoresponse dynamic behavior can be seen. Then, the four-stage response behavior is schematically analyzed in Fig. 3g. Under the dark condition, the spontaneous polarization within the PbI_2/Pb(SCN)$_2$ perovskite film along the normal direction generates positive polarization charges at the interface between perovskite and ITO and negative charges at the p-n junction interface. Correspondingly, opposite free charges will be generated in the ITO electrode and P3HT. When the 532 nm laser is turned on, the light-induced carriers will be generated and separated by the built-in field induced by p-n junction and ferroelectricity, resulting in the photocurrent (I_{photo}). Besides, the light-induced temperature rise will disturb the random oscillation state of electric dipoles within the 1D/3D perovskite mixed film as a result of increased thermal vibrations, resulting in the decreased ferroelectric polarization charges [12–14,30]. Therefore, the free charges flow will generate the positive output pyroelectric current (I_{pyro}). This positive current is defined as $I_{pyro+photo}$. When the temperature remains unchanged, the pyroelectric current will vanish, only leaving stable photocurrent plateau. When the laser is turned off, the temperature decrease of the PDs will lead to the increased bound charges, generating reversed pyroelectric current ($I_{pyro'}$). The light-induced changes of ferroelectric polarized charge will modulate the charge carriers' photoelectric process at the interface, enhancing the optoelectronic performances. The working mechanism is also analyzed using the schematic energy band diagrams of the PD under dark, and light illumination conditions in Fig. 3h and 3i, respectively. When 532 nm lasers are illuminated on the PbI_2/Pb(SCN)$_2$ perovskite film, photovoltaic effect-induced charge carriers will be generated and an immediate temperature rise induced by light will lead to the decreased ferroelectric negative polarization charges distributed at the p-n junction interface between $MAPbI_3$ and P3HT. The less negative charges are beneficial for attracting the electrons in the $MAPbI_3$ migrating to the interface and driving the holes in the p-type P3HT away from the interface, resulting in a downward bending of the energy band (orange lines), lowering the barrier height, beneficial for the transport of light-induced electrons and holes. To further confirm the existence of pyroelectricity, the *I-t* curves of the PD under dark conditions by raising the temperature (using a 10.6 μm CO_2 laser as the heating source) are measured (Fig. S17), from which one can see that positive current peaks

appeared when the temperature was increased. When the laser was turned off, the temperature dropped, leading to a negative pyroelectric current.

Then, the photoresponses of the $PbI_2/Pb(SCN)_2$-TMIMI perovskite-based PD and two control PDs were systemically measured. Fig. 4 systematically evaluates the photoresponses of the $PbI_2/Pb(SCN)_2$ perovskite-based PD towards 532 nm laser illumination. The zero biased *I-t* curves with power density ranging from 0.013 to 25.48 mW/cm^2 are shown in Fig. 4a. When the power density is low ($\leq$ 0.13 mW/cm^2), four-stage dynamic behaviors are obvious (inset of Fig. 4a). When the power density increases, the negative pyroelectric currents gradually become inconspicuous while the positive pyroelectric currents continuously rise. The relative peak-to-peak current ($I_{pyro+photo}$-$I_{pyro'}$), the positive peak current $I_{pyro+photo}$, and plateau current I_{photo} are extracted from Fig. 4a and drawn as a function of power density in Fig. 4b. All the three output currents increase linearly with the power density. It can be seen that the ferro-pyro-phototronic effect signicantly raises the pyroelectric currents $I_{pyro+photo}$-$I_{pyro'}$ and $I_{pyro+photo}$ in comparison to I_{photo} (Fig. 4d). Then the responsivities (R) and detectivities (D^*) are calculated following the following equations:

$$R\lambda = \frac{J_p - J_d}{P_\lambda} \tag{2}$$

$$D* = \frac{(BS)^{1/2}}{NEP} = \frac{R_\lambda (BS)^{1/2}}{\overline{i_n^2}^{1/2}} \tag{3}$$

where J_p is the output current density under light illumination, J_d is the dark current density, P_λ is the laser power density, S is the effective area, B is the bandwidth, *NEP* is the noise equivalent power, $\overline{i_n^2}^{1/2}$ is the root mean square value of the noise current. The noise level per unit bandwidth (1 Hz) of the photodetectors can be deduced from Fig. S13. Then, three R_λ and D^* are calculated and plotted in Fig. 4c and 4e, respectively. As shown in Fig. 4c, all the three curves show a similar tendency with the increase of power density. The maximum $R_{pyro+photo-pyro'}$ of 5.66 mA/W occurs with a power density of 12.74 mW/cm^2, while the maximum R_{photo} is 3 mA/W (Fig. 4d). Here, I_d is about 7.7 nA (Fig. S7), and S is 0.785 cm^2. As shown in Fig. 4e, the maximum detectivity $D^*_{pyro+photo-pyro'}$ is about 1×10^{10} Jones. We also measured the photovoltage response of the PD under 532 nm illumination (Fig. S18), showing the self-powered photodetecting ability of the PDs.

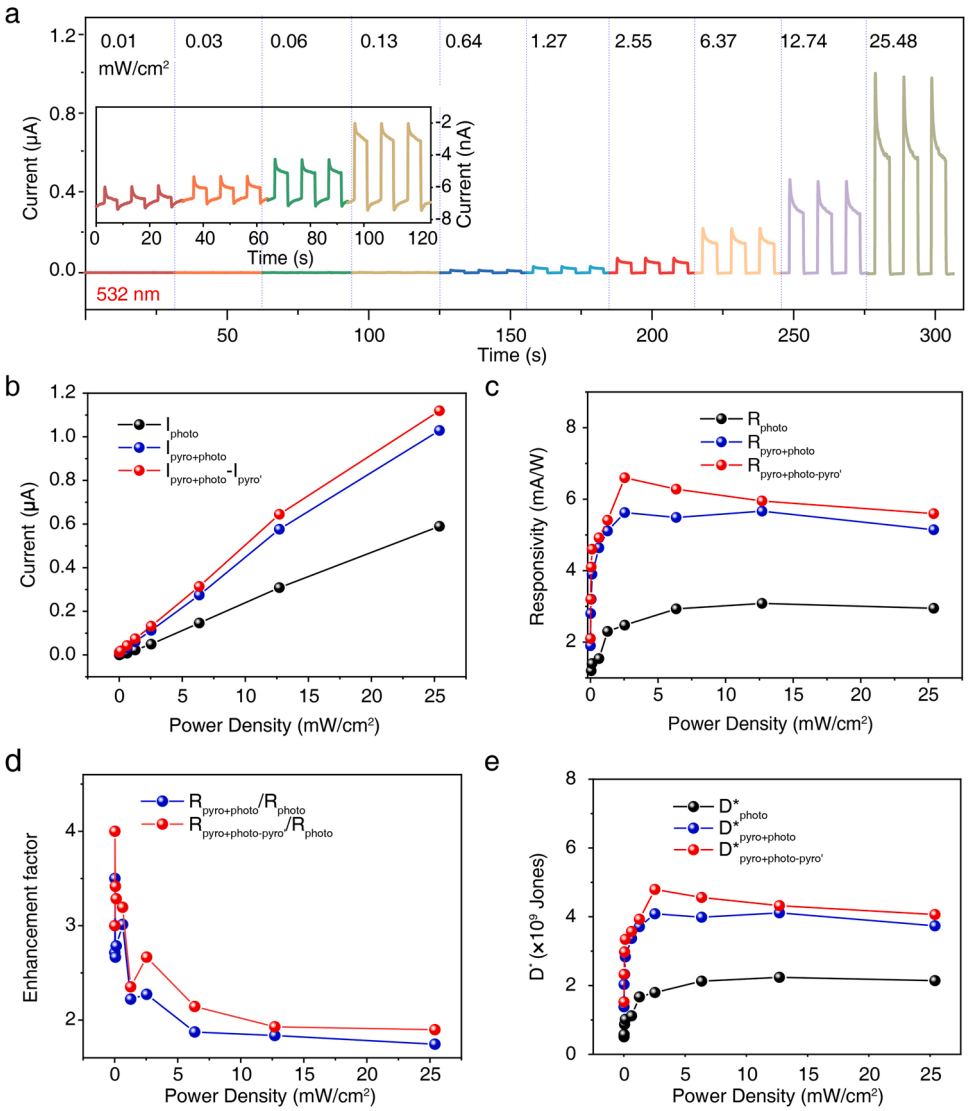

Fig. 4. (a) On-off photo-responses of the $PbI_2/Pb(SCN)_2$-TMIMI perovskite-based PD towards 532 nm laser with different power densities. (b) $I_{pyro+photo}$-$I_{pyro'}$, $I_{pyro+photo}$, and I_{photo}, (c) corresponding $R_{pyro+photo-pyro'}$, $R_{pyro+photo}$, and R_{photo}, (d) enhancement factor for ($R_{pyro+photo-pyro'}$)/R_{photo} and $R_{pyro+photo}/R_{photo}$ and (e) D^* as a function of the power density.

Similar results for photo-responses of the PbI_2/Pb(SCN)$_2$-TMIMI perovskite-based PD towards 360, 450, and 785 nm laser illumination with zero bias are demonstrated in Fig. S19-S21, respectively, indicating that the universality of ferro-pyro-phototronic effect in enhancing the PDs' performance. Fig. S22 shows the $R_{pyro+photo-pyro'}$ of the PD towards 360, 450, 532 and 785 nm laser as a function of power density, further confirming the photoresponse the PD could be improved by the ferro-pyro-phototronic effect in a broad spectral range. The photoresponses of the PbI_2/Pb(SCN)$_2$ perovskite and PbI_2 perovskite-based PDs were measured and plotted in Fig. S23-S24, respectively. There exist weak pyroelectric currents for PbI_2 perovskite-based PD (inset of Fig. S23a), since $MAPbI_3$ has been proven to have a secondary pyroelectric effect in our early report [31]. The four-stage photo-response dynamic behavior becomes more evident for PbI_2/Pb(SCN)$_2$ perovskite due to the larger grain size and enhanced crystallinity (Fig. S24).

As shown in Fig. S25, the response time of the PbI_2/Pb(SCN)$_2$-TMIMI based PD was determined as 0.35 ms for the rise and 0.36 ms for the decay under an irradiance of 12.7 mW/cm^2, which are shorter than those for the other two devices. The relatively slow response speeds may be attributed to the imperfect interfaces which hinders the extraction rate of light-induced carriers. Fig. S26 compared the overall photo-response performances of the three PDs, directly proving the advantage of the PbI_2/Pb(SCN)$_2$-TMIMI based PD. The polarization direction switching of the ferroelectric films allow the modulation of output current directions. As shown in Fig. S27a, after poled with opposite polarization voltage of -1 V, opposite pyroelectric currents are observed when light is turned on. Furthermore, the signals of the open-circuit voltage (V_{oc}) are opposite with different polarization orientations (Fig. S27b). These features suggest that the self-powered photodetection performance of our devices is related to the ferroelectric properties. From the above results, we can find the superiority of the combination of 1D ferroelectric perovskite doping and non-halide engineering. The photodetection performances of the previously reported self-powered reported pyro-phototronic effect-based PDs, and the present ^{1}D–^{3}D ferroelectric film-based PD are listed in Table 1, from which one can see that our PDs demonstrate the medium levels of photoresponsivity and detectivity.

In addition, we also evaluate the impact of bias voltage on photo-sensing performance. Fig. S28 shows the *I-t* curves under reverse bias voltages ranging from 0 to 1.6 V and forward bias voltages ranging from 0 to 1.6 V towards 532 nm illumination (6.37 mW/cm^2). With the increase of reverse bias, the photocurrent is gradually enhanced while the pyroelectric currents gradually decrease and finally vanish when the bias exceeds 1.4 V. However, with the increase of forward bias from 0.2 V to 0.8 V, the photocurrent gradually decreases while the four-stage photo-response dynamic behavior becomes more obvious and the pyroelectric current gradually increases. At a forward bias of 0.8 V, the pyroelectric current reaches a maximum value. Then, with the further increase of forward bias voltage, the pyroelectric response gradually decrease and finally vanishes at 1 V.

The PbI_2/Pb(SCN)$_2$-TMIMI perovskite-based PDs also showed excellent folding endurance. Fig. 5a shows the on-off photoresponse of the flexible device at bending angles of 0° and 30°, respectively, under the same laser illumination (532 nm, mW/cm^2). The PDs also maintain appreciable photoresponses (80% compared with the 0° condition) at bending angle of 30°. Moreover, the on-off photoresponse was examined after different bending cycles from 0 to 1000, with less than 2% degradation of the photocurrents and pyroelectric currents (Fig. 5b). The output currents and response speeds remain almost unchanged even after 1000 bending cycles, demonstrating strong folding endurance. The enhanced folding endurance should be attributed to the existence of 1, 3-DAP which acts as a glue between grains and improve adhesion between perovskite and ITO since -NH_2 can participate in hydrogen bonding with the [PbI_6] octahedral framework and the underlying polyethylneimine (PEIE) layer, thus reducing the cracking and peeling-off possibility of the perovskite film during bending[22]. Moreover, our PDs exhibited excellent anti-humidity stability. As shown in Fig. 5c and d, the devices experienced decay of photoresponse dynamics, maintaining 100% of their initial photo current after being stored in ambient air (80 ± 5% RH) at RT for 39 days. While the pyroelectric response retains 82% of the initial value. The photocurrent increased first and then declined gradually, then remained steady. This phenomenon may be caused by device aging, which is also found in the reported article [38]. Besides, the device maintained 99.6% of the initial photocurrent value after being exposed to air for more than 64 d, as shown in Fig. S29. Furthermore, the PDs also demonstrated good reproducibility. We measured over 10 PDs' on-off photo-responses to evaluate the PDs' performances. Fig. S30 depicts averaged lowest detectable power density and maximum responsivity of the PDs, with relatively small distributions, showing good consistency.

3. Conclusion

In summary, we successfully fabricated a self-powered, flexible, and ultra-stable photodetector based on highly crystalized 1D/3D ferroelectric perovskite mixed film which relies on the ferro-pyro- phototronic effect. It is found that the combination of doping with 1D ferroelectric perovskite and non-halide engineering significantly improves the crystallinity and reduces the trap densities. Thus, excellent photoresponse performance is realized. The corresponding responsivity and response speed of the PbI_2/Pb(SCN)$_2$-TMIMI perovskite-based PDs can be boosted compared with PbI_2 perovskite-based PD. The enhanced performance could be attributed to the ferro-pyro-phototronic effect of the 1D/3D ferroelectric perovskite due to the modulation of ferroelectric polarization charges on the carrier photoelectric process near the p-n junction interface. This work not only offers a simple and effective method to achieve high-performance and self-powered PDs, but also provides a potential for future wearable or portal optoelectronics.

Table 1
Performance comparisons of reported pyro-phototronic effect based self-powered photodetectors.

Active Materials	Wavelength (nm)	Responsivity (mA W^{-1})	Detectivity (Jones)	Rise time (s)	Decay time (s)	Ref.
CdS/Si	325	5.9	1.0×10^{12}	$\sim 2.5 \times 10^{-4}$	$\sim 2.7 \times 10^{-4}$	[10]
ZnO/CuO p–n Junction	325	0.14	3.3×10^{11}	0.01	0.01	[11]
$BaTiO_3$ film	405	7.5×10^{-3}	$\sim 9 \times 10^{9}$	0.88	1.06	[12]
$BaTiO_3$/GaN Heterojunction	325	—	—	0.16	2.53	[13]
(hexylammonium)$_2CsPb_2Br_7$	405	—	—	1.5	3.6	[16]
$(PMA)_2PbCl_4$	320	9000	1.01×10^{11}	1.62×10^{-4}	2.26×10^{-4}	[17]
ZnO NWs/SnS	365	0.155	—	49.1	51.8	[32]
ZnO/PLZT heterojunction	360	3.96	6.6×10^{10}	0.04	0.05	[33]
Si/SnO_x/ZnO heterojunction	650	64.1	1.5×10^{11}	3×10^{-6}	2×10^{-6}	[34]
SnS/CdS Heterojunction	650	10.4	3.56×10^{11}	0.03	—	[35]
p-Si/n-ZnO Heterojunction	785	17.9	2.93×10^{9}	2×10^{-3}	1.8×10^{-3}	[36]
PbI_2/Pb(SCN)$_2$-TMIMI perovskite	532	6.6	5×10^{9}	0.035	0.036	This work

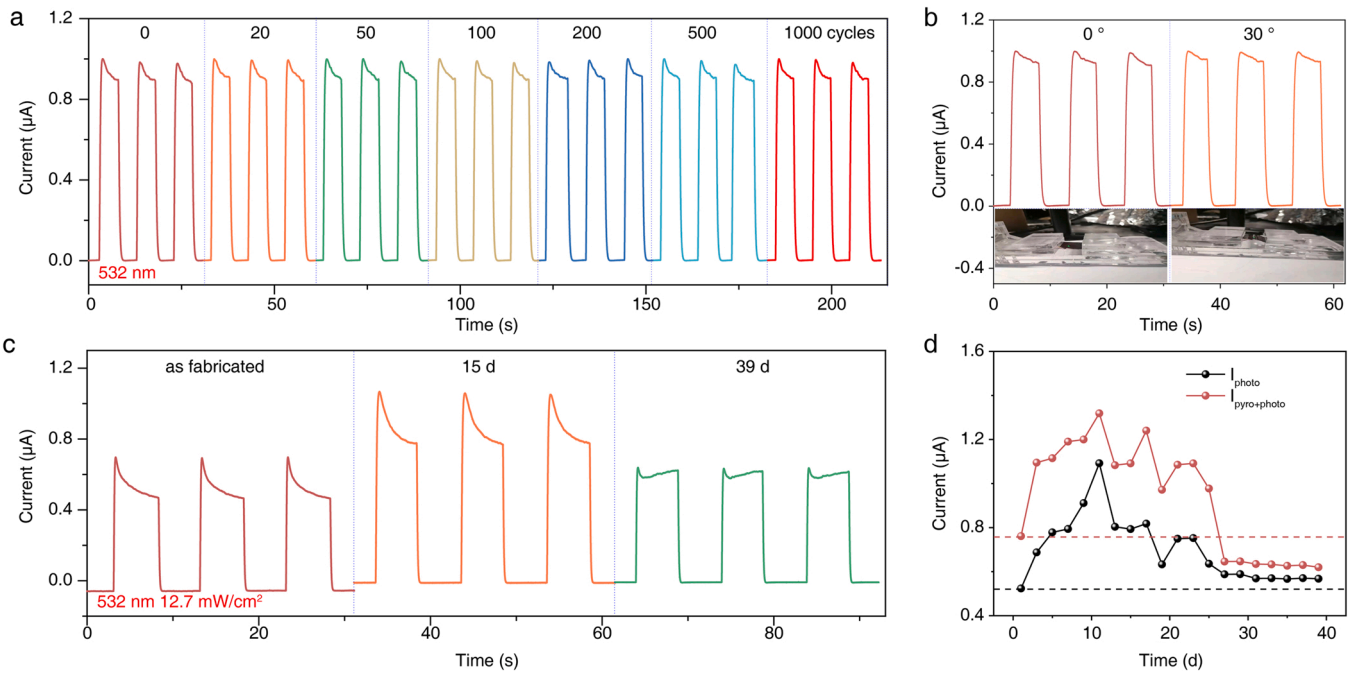

Fig. 5. (a) Time-dependent on/off switching behavior of the flexible PD before and after 20, 50, 100, 200, 500, and 1000 bending cycles and (b) the transient photo-response with different bending angles, 0° (red lines) and 30° (orange lines), respectively, illuminated by 532 nm laser with 12.7 mW/cm^2. The insets are the corresponding photographs of the device with different bending angles. c) The transient photo-response of PD without encapsulation exposed to air conditions (80 ± 10% RH and RT) in the dark. (d) The corresponding output currents of the PD to the 532 nm laser illumination (12.7 mW/cm^2) after 0 and 39 days.

4. Experimental section

Materials: The SnO_2 colloid solution oxide (15 wt% in H_2O colloidal dispersion), N, N-Dimethylformamide (DMF, 99.9%), 1, 3-DAP (99.9%), PEIE (80% ethoxylated solution), chlorobenzene (99.5%), cyclohexane (99.5%) and tert-amyl alcohol (99.5%) were purchased from Shanghai Macklin Biochemical Co., Ltd. PbI_2 (99.99%), $Pb(SCN)_2$ (99.99%), methylammonium iodide (MAI, 99.99%), methylammonium acetate (MAAc, 99.99%), [6,6]-Phenyl C61 butyric acid methyl ester (PC61BM), poly(3-hexylthiophene-2, 5-diyl) (P3HT), poly[(9, 9-dioctylfluorenyl-2, 7-diyl)-alt-(4, 4′-(N-(4-butylphenyl) (TFB), and poly(3, 4-ethylenedioxythiophene)-poly(styrenesulfonate) (PEDOT:PSS 1000) were purchased from Xian Polymer light Technology Corp. Indium tin oxide (ITO)/polyethylene naphthalate (PEN) substrate (sheet resistance ≤ 6 Ω) were purchased from South China Science & Technology Co., Ltd. All the chemicals were used as received without further purification. TMIMI was synthesized following the reported result [24].

Preparation of precursor solution: A series of 0.56 M perovskite precursor solutions were prepared by dissolving 0.56 M lead salt PbI_2/$Pb(SCN)_2$ with variable proportions (1:0, 0:1, 1:1, 3:1, 7:1 and 9:1) and MAI in MAAc and stirring at 60 °C for 12 h. The insufficient iodide ions were offered by adding extra MAI. The extra MA^+ will be removed as MASCN during the spin-coating and annealing procedure. For 1D/3D perovskite mixed films, 0.65 mol% (3.6 mM) TMIMI was added into the precursor solution simultaneously. Further added TMIMI couldn't be dissolved. Then, 1, 3-DAP was dissolved in DMF separately and added to the as-prepared perovskite solution at a concentration of 0.025 wt%.

Fabrication of the PDs: The devices with a structure of PEN/ITO/PEIE/$MAPbI_3$/P3HT/Au were fabricated in ambient air (temperature~23 °C, RH~40%). Firstly, PEN/ITO substrates were ultrasonically washed in acetone, ethanol, and deionized water for 15 min successively. After being blew with dry N_2 flow, the substrates were treated with O_2 plasma (80 W) for 10 min. Then the substrates were treated with PEIE solution following the literature to enhance the wettability of MAAc [37]. Briefly, the ITO/PEN substrates were fully immersed in 0.4 wt% PEIE aqueous solution for 30 s and then rinsed in deionized water for 3 s, followed by thermal annealing at 100 °C for 10 min. The perovskite precursor solution was then spin-coated at 4000 rpm for 20 s at a constant 90 °C during the whole spin-coating process. After gradient annealing at 60 °C for 2 min and 100 °C for 3 min, the perovskite films were cleaned and healed according to the literature with some modifications [39]. Cleaning solutions were prepared by mixing cyclohexane and tert-amyl alcohol in a volume ratio of 4:1. Healing solutions were prepared by adding 0.2 mg/mL MAI and 0.2 mg/mL TEA to the above solutions. Here, as a moisture-tolerant molecule, TEA can be assembled on the perovskite surface as effcient water-resisting layers [40]. Then, P3HT in chlorobenzene solution (10 mg/mL) was deposited onto the perovskite films. Finally, 80 nm Au was deposited by a thermal evaporator (0.5 Å/s) using a shadow mask. 3 nm Ni was deposited before the Au layer to enhance the adhesion of the Au electrode.

Characterization: XRD patterns were obtained by the Bruker D8 Advance X-ray diffractometer equipped with a Cu tube (λ = 1.5406 Å). UV–vis absorbance spectrum was measured using a Hitachi U4100 UV-Vis-NIR spectrophotometer at RT, with a wavelength range of 250–800 nm. UPS measurements were recorded using a photoelectron spectrometer (Thermo, ESCALAB 250 Xi) to analyze the working function of the perovskite films. Steady-state and time-resolved PL measurements were taken using an FLS920 (Edinburgh Instruments) fluorescence spectrometer with a 325 nm excitation wavelength. The morphological analyses of the films and devices were examined by conducting scanning electron microscopy (Nova NanoSEM450).

SCLC measurements: Trap-state densities were determined using the SCLC method. The structure is ITO/PEDOT:PSS/perovskite/TFB/Au for hole-only devices. PEDOT:PSS solution was spin-coated at 5000 rpm for 60 s and PEDOT:PSS was spin-coated on the ITO at 5000 rpm for 60 s in air and then annealed at 150 °C for 30 min. After the spin coating of the perovskite layer, the TFB layer (8 mg/mL in chlorobenzene) was spin-coated at 2000 rpm for 60 s. Finally, the 80 nm Au electrode was deposited using thermal evaporation through a shadow mask. The structure is ITO/SnO_2/perovskite/PC61BM/Ag for electron-only devices. The dilute SnO_2 solution (2.5 wt%) was spin-coated on the ITO at

3000 rpm for 30 s and annealed at 150 °C for 30 min. After the spin coating of the perovskite layer, the PC61BM layer (10 mg/mL in chlorobenzene) was spin-coated at 2000 rpm for 60 s. Finally, the 80 nm Au electrode was deposited using a thermal evaporation through a shadow mask. The dark *I-V* curves were obtained using the Keithley 4200 source meter.

Photodetection performance measurements: The *I-V* characteristics and the *I-t* curves of the PDs were recorded by coupling a Stanford SRS current preamplifier (SR570) and a Stanford SRS function generator (DS345). The temporal responses of the device were performed on a digital oscilloscope (Tektronix, MDO3104). The laser was periodically switched by transistor-transistor logic (TTL) potential to generate pulsed laser beams. The 360, 450, 532, and, 785 lasers (Changchun New Industries Optoelectronics Technology Co., Ltd.) were used as the light sources and shined from the back of the PDs. The light power intensity was calibrated employing a silicon photodiode (PM100D). All PDs were stored in the ambient atmosphere without any encapsulation during the measurements.

Stability test: The humidity stability of the unencapsulated PDs were performed by storing devices in 80 ± 10%RH condition at RT. All PDs were tested under 532 nm laser illumination for *I-t* characterization at regular intervals. The RH in the laboratory was within 30 ± 10% during the entire test.

CRediT authorship contribution statement

Zheng Yang: Writing – original draft preparation, Writing – review & editing, Investigation, Formal analysis, Methodology, Software. **Xiaoli Li:** Investigation, Formal analysis, Software. **Linjie Gao:** Writing – review & editing, Funding acquisition. **Wei Zhang:** Investigation, Resources. **Xinzhan Wang:** Investigation, Resources. **Haixu Liu:** Investigation, Resources. **Shufang Wang:** Resources, Validation, Funding acquisition. **Caofeng Pan:** Supervision, Validation, Funding acquisition. **Linjuan Guo:** Project administration, Supervision, Writing – review & editing, Funding acquisition.

Declaration of Competing Interest

The authors declare that they have no known competing financial interests or personal relationships that could have appeared to influence the work reported in this paper.

Data Availability

No data was used for the research described in the article.

Acknowledgment

This work was supported by the National Natural Science Foundation of China (Grant Nos. 62005072, 62104057, 51972094, 52125205, U20A20166, 61805015 and 61804011), the Natural Science Foundation of Hebei Province (Grant Nos. E2020201025, E2021201016, and B2021201034), Hebei Education Department (Grant No. BJK2022050), the Advanced Talents Incubation Program of the Hebei University (521000981287, 521000981351, and 521000981248), the Undergraduate Innovation and Entrepreneurship Training Program of the Hebei University (2021174 and 2021172), the Science and Technology Plan Project of Hebei Province (Grant No. 226Z1002G).

Appendix A. Supporting information

Supplementary data associated with this article can be found in the online version at doi:10.1016/j.nanoen.2022.107743.

References

[1] J. Feng, C. Gong, H. Gao, W. Wen, Y. Gong, X. Jiang, B. Zhang, Y. Wu, Y. Wu, H. Fu, L. Jiang, X. Zhang, Single-crystalline layered metal-halide perovskite nanowires for ultrasensitive photodetectors, Nat. Electron. 1 (2018) 404–410.
[2] J.J. Yoo, G. Seo, M.R. Chua, T.G. Park, Y. Lu, F. Rotermund, Y.K. Kim, C.S. Moon, N.J. Jeon, J.P. Correa-Baena, V. Bulovic, S.S. Shin, M.G. Bawendi, J. Seo, Efficient perovskite solar cells via improved carrier management, Nature 590 (2021) 587–593.
[3] E. Shi, B. Yuan, S.B. Shiring, Y. Gao, Y. Akriti, C. Guo, M. Su, P. Lai, J. Yang, B. M. Kong, Y. Savoie, L. Yu, Dou, Two-dimensional halide perovskite lateral epitaxial heterostructures, Nature 580 (2020) 614–620.
[4] Z. Li, X. Liu, C. Zuo, W. Yang, X. Fang, Supersaturation-controlled growth of monolithically integrated lead-free halide perovskite single-crystalline thin film for high-sensitivity photodetectors, Adv. Mater. 33 (2021) 2170324.
[5] Z. Han, W. Fu, Y. Zou, Y. Gu, J. Liu, B. Huang, D. Yu, F. Cao, X. Li, X. Xu, H. Zeng, Oriented perovskite growth regulation enables sensitive broadband detection and imaging of polarized photons covering 300–1050 nm, Adv. Mater. 33 (2021) 2003852.
[6] Y. Hou, C. Wu, X. Huang, D. Yang, T. Ye, J. Yoon, R. Sriramdas, K. Wang, S. Priya, Self-powered red/UV narrowband photodetector by unbalanced charge carrier transport strategy, Adv. Funct. Mater. 31 (2020), 202007016.
[7] X. Hu, X. Li, G. Li, T. Ji, F. Ai, J. Wu, E. Ha, J. Hu, Recent progress of methods to enhance photovoltaic effect for self-powered heterojunction photodetectors and their applications in inorganic low-dimensional structures, Adv. Funct. Mater. 31 (2021) 2011284.
[8] L. Li, Y. Zhang, R. Wang, J. Sun, Y. Si, H. Wang, C. Pan, Y. Dai, Ferroelectricity-induced nduced performance enhancement of V-doped ZnO/Si photodetector by direct energy band modulation, Nano Energy 65 (2019), 104046.
[9] F. Cao, W. Tian, M. Wang, H. Cao, L. Li, Semitransparent, flexible, and self-powered photodetectors based on ferroelectricity-assisted perovskite nanowire arrays, Adv. Funct. Mater. 29 (2019) 1901280.
[10] Y. Dai, X. Wang, W. Peng, C. Xu, C. Wu, K. Dong, R. Liu, Z.L. Wang, Self-powered Si/CdS flexible photodetector with broadband response from 325 to 1550 nm based on pyro-phototronic effect: an approach for photosensing below bandgap energy, Adv. Mater. 30 (2018) 1705893.
[11] Q. Li, J. Meng, J. Huang, Z. Li, Plasmon-induced pyro-phototronic effect enhancement in self-powered UV-vis detection with a ZnO/CuO p-n junction device, Adv. Funct. Mater. 32 (2021) 2108903.
[12] K. Zhao, B. Ouyang, C.R. Bowen, Y. Yang, Enhanced photocurrent via ferro-pyro-phototronic effect in ferroelectric $BaTiO_3$ materials for a self-powered flexible photodetector system, Nano Energy 77 (2020), 105152.
[13] Y. Zhang, J. Chen, L. Zhu, Z.L. Wang, Self-powered high-responsivity photodetectors enhanced by the pyro-phototronic effect based on a $BaTiO_3$/GaN heterojunction, Nano Lett. 21 (2021) 8808–8816.
[14] Y. Liu, X. Pan, X. Liu, S. Han, J. Wang, L. Lu, H. Xu, Z. Sun, J. Luo, Tailoring Interlayered spacers of two-dimensional cesium-based perovskite ferroelectrics toward exceptional ferro-pyro-phototronic effects, Small 18 (2022) 2106888.
[15] Y. Zhang, E. Parsonnet, A. Fernandez, S.M. Griffin, H. Huyan, C.-K. Lin, T. Lei, J. Jin, E.S. Barnard, A. Raja, P. Behera, X. Pan, R. Ramesh, P. Yang, Ferroelectricity in a semiconducting all-inorganic halide perovskite, Sci. Adv. 8 (2022) 5881.
[16] Z. Xu, W. Weng, Y. Li, X. Liu, T. Yang, M. Li, X. Huang, J. Luo, Z. Sun, 3D-to-2D dimensional reduction for exploiting a multilayered perovskite ferroelectric toward polarized-light detection in the solar-blind ultraviolet region, Angew. Chem. Int. Ed. Engl. 59 (2020) 21693–21697.
[17] L. Guo, X. Liu, L. Gao, X. Wang, L. Zhao, W. Zhang, S. Wang, C. Pan, Z. Yang, Ferro-pyro-phototronic effect in monocrystalline 2D ferroelectric perovskite for high-sensitive, self-powered, and stable ultraviolet photodetector, ACS Nano 16 (2022) 1280–1290.
[18] H. Zhang, Z. Shi, L. Hu, Y.Y. Tang, Z. Qin, W.Q. Liao, Z.S. Wang, J. Qin, X. Li, H. Wang, M. Gusain, F. Liu, Y. Pan, M. Xu, J. Wang, R. Liu, C. Zhang, R.G. Xiong, W.E.I. Sha, Y. Zhan, Highly efficient 1D/3D ferroelectric perovskite solar cell, Adv. Funct. Mater. 31 (2021), 2100205.
[19] C. Liang, H. Gu, Y. Xia, Z. Wang, X. Liu, J. Xia, S. Zuo, Y. Hu, X. Gao, W. Hui, L. Chao, T. Niu, M. Fang, H. Lu, H. Dong, H. Yu, S. Chen, X. Ran, L. Song, B. Li, J. Zhang, Y. Peng, G. Shao, J. Wang, Y. Chen, G. Xing, W. Huang, Two-dimensional Ruddlesden-Popper layered perovskite solar cells based on phase-pure thin films, Nat. Energy 6 (2020) 38–45.
[20] H. Xu, S. Han, Z. Sun, J. Luo, Recent advances of two-dimensional organic-inorganic hybrid perovskite ferroelectric materials, Acta Chim. Sin. 79 (2021) 23–35.
[21] L. Chao, Y. Xia, B. Li, G. Xing, Y. Chen, W. Huang, Room-temperature molten salt for facile fabrication of efficient and stable perovskite solar cells in ambient air, Chem 5 (2019) 995–1006.
[22] Z. Wang, J. Jin, Y. Zheng, X. Zhang, Z. Zhu, Y. Zhou, X. Cui, J. Li, M. Shang, X. Zhao, S. Liu, Q. Tai, Achieving efficient and stable perovskite solar cells in ambient air through non-halide engineering, Adv. Energy Mater. 11 (2021) 2102169.
[23] W.-Q. Wu, Z. Yang, P.N. Rudd, Y. Shao, X. Dai, H. Wei, J. Zhao, Y. Fang, Q. Wang, Y. Liu, Y. Deng, X. Xiao, Y. Feng, J. Huang, Bilateral alkylamine for suppressing charge recombination and improving stability in blade-coated perovskite solar cells, Sci. Adv. 5 (2019) 8925.
[24] X.N. Hua, W.Q. Liao, Y.Y. Tang, P.F. Li, P.P. Shi, D. Zhao, R.G. Xiong, A. Room-Temperature, Hybrid lead iodide perovskite ferroelectric, J. Am. Chem. Soc. 140 (2018) 12296–12302.

[25] P. Liu, Y. Xian, W. Yuan, Y. Long, K. Liu, N.U. Rahman, W. Li, J. Fan, Lattice-matching structurally-stable 1D@3D perovskites toward highly efficient and stable solar cells, Adv. Energy Mater. 10 (2020) 1903654.
[26] Y. Song, W. Bi, A. Wang, X. Liu, Y. Kang, Q. Dong, Efficient lateral-structure perovskite single crystal solar cells with high operational stability, Nat. Commun. 11 (2020) 274.
[27] Q. Dong, Y. Fang, Y. Shao, P. Mulligan, J. Qiu, L. Cao, J. Huang, Solar cells. Electron-hole diffusion lengths > 175 mum in solution-grown CH3NH3PbI3 single crystals, Science 347 (2015) 967–970.
[28] Q. Lai, L. Zhu, Y. Pang, L. Xu, J. Chen, Z. Ren, J. Luo, L. Wang, L. Chen, K. Han, P. Lin, D. Li, S. Lin, B. Chen, C. Pan, Z.L. Wang, Piezo-phototronic effect enhanced photodetector based on $CH_3NH_3PbI_3$ single crystals, ACS Nano 12 (2018) 10501–10508.
[29] C.-H. Liu, Y.-C. Chang, T.B. Norris, Z. Zhong, Graphene photodetectors with ultra-broadband and high responsivity at room temperature, Nat. Nanotechnol. 9 (2014) 273–278.
[30] Y. Zhang, P. Pham Thi Thuy, E. Roake, H. Khanbareh, Y. Wang, S. Dunn, C. Bowen, Thermal energy harvesting using pyroelectric-electrochemical coupling in ferroelectric materials, Appl. Phys. 4 (2020) 301–309.
[31] Z. Yang, H. Wang, L. Guo, Q. Zhou, Y. Gu, F. Li, S. Qiao, C. Pan, S. Wang, A. Self-Powered, Photodetector based on $MAPbI_3$ single-crystal film/n-Si heterojunction with broadband response enhanced by pyro-phototronic and piezo-phototronic effects, Small 17 (2021) 2101572.
[32] B. Ouyang, K. Zhang, Y. Yang, Photocurrent polarity controlled by light wavelength in self-powered ZnO nanowires/SnS photodetector system, IScience 1 (2018) 16–23.
[33] J. Chen, Z. Wang, H. He, J. Mao, Y. Zhang, Q. Zhang, M. Li, Y. Lu, Y. He, High-performance self-powered ultraviolet photodetector based on coupled ferroelectric depolarization field and heterojunction built-in potential, Adv. Electron. Mater. 7 (2021) 2100717.
[34] J.P.B. Silva, E.M.F. Vieira, K. Gwozdz, A. Kaim, L.M. Goncalves, J.L. MacManus-Driscoll, R.L.Z. Hoye, M. Pereira, High-performance self-powered photodetectors achieved through the pyro-phototronic effect in Si/SnOx/ZnO heterojunctions, Nano Energy 89 (2021), 106347.
[35] Y. Chang, J. Wang, F. Wu, W. Tian, W. Zhai, Structural design and pyroelectric property of SnS/CdS heterojunctions contrived for low-temperature visible photodetectors, Adv. Funct. Mater. 30 (2020) 2001450.
[36] Y. Zhang, M. Hu, Z. Wang, Enhanced performances of p-Si/n-ZnO self-powered photodetector by interface state modification and pyro-phototronic effect, Nano Energy 71 (2020), 104630.
[37] X. Min, F. Jiang, F. Qin, Z. Li, J. Tong, S. Xiong, W. Meng, Y. Zhou, Polyethylenimine aqueous solution: a low-cost and environmentally friendly formulation to produce low-work-function electrodes for efficient easy-to-fabricate organic solar cells, ACS Appl. Mater. Interfaces 6 (2014) 22628–22633.
[38] L. Min, W. Tian, F. Cao, J. Guo, L. Li, 2D Ruddlesden-Popper perovskite with ordered phase distribution for high-performance self-powered photodetectors, Adv. Mater. 33 (2021) 2101714.
[39] X.-J. She, C. Chen, G. Divitini, B. Zhao, Y. Li, J. Wang, J.F. Orri, L. Cui, W. Xu, J. Peng, S. Wang, A. Sadhanala, H. Sirringhaus, A solvent-based surface cleaning and passivation technique for suppressing ionic defects in high-mobility perovskite field-effect transistors, Nat. Electron. 3 (2020) 694–703.
[40] S. Yang, Y. Wang, P. Liu, Y.-B. Cheng, H.J. Zhao, H.G. Yang, Functionalization of perovskite thin films with moisture-tolerant molecules, Nat. Energy 1 (2016) 15016.

Dr. Zheng Yang received his Ph.D. degree in Nanoscience and Nanotechnology from the Beijing Institute of Nanoenergy and Nanosystems (CAS) in 2019. Then he joined the College of Physics Science and Technology at Hebei University. His research is mainly focused on the controllable growth and optoelectronics applications of lead halide perovskites.

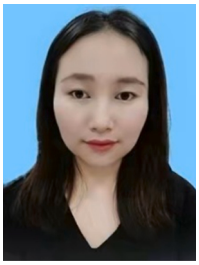

Xiaoli Li received her bachelor's degree from Tianshui Normal University in 2020. She is currently a graduate student in the School of Physical Science and Technology, Hebei University. Her research interest is mainly focused on perovskite photodetectors based on pyro-phototronic effect.

Dr. Linjie Gao received her Ph.D. degree from Hebei University in 2018. Then she joined the College of Physics Science and Technology at Hebei University. Her research is mainly focused on the design and controllable preparation of photothermal materials.

Dr. Wei Zhang received his Ph.D degree from Soochow University in 2016. He then joined the College of Physics Science and Technology at Hebei University. His research interests include magnetoelectric functional materials, 2D materials, as well as their electronic and and optoelectronic devices.

Dr. Xinzhan Wang received his Ph.D. degree in Optical Engineering from Hebei University in 2014. Then he joined the College of Physics Science and Technology at Hebei University. His research is mainly focused on the optoelectronic applications of lead halide perovskites.

Dr. Haixu Liu received his Ph.D. degree in Condensed matter physics from the Nankai University (NKU) in 2011. Then he joined the College of Physics Science and Technology at Hebei University. His research interest is mainly focused on the preparation of novel optoelectronics thin films and the fabrication of long-term stable perovskites solar cells (PSCs).

Dr. Shufang Wang received her Ph.D. degree in Optics from the Institute of Physics, Chinese Academy of Sciences in 2004. She then joined in the group of Professor D. Rémiens at IEMN-CNRS, France as a postdoctral fellow and after that joined in the group of Professor Xiaoxing Xi at the Penn. State University as a postdoctral fellow. She is currently a full professor and a group leader at Hebei University of China. Her researches focus on the fields of photoelectric/thermoelectric materials and devices.

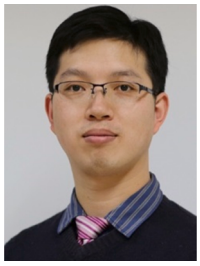

Dr. Caofeng Pan received his B.S. degree (2005) and his Ph.D. (2010) in Materials Science and Engineering from Tsinghua University, China. He then joined the Georgia Institute of Technology as a postdoctoral fellow. He is currently a professor and a group leader at the Beijing Institute of Nanoenergy and Nanosystems, Chinese Academy of Sciences since 2013. His main research interests focus on the fields of piezotronics/piezo-phototronics for fabricating new electronic and opto-electronic devices, nano-power sources (such as nanofuel cell, nano biofuel cell and, nanogenerator), hybrid nanogenerators, and self-powered nanosystems. Details can be found at http://piezotronics.binncas.cn/index%20en.php.

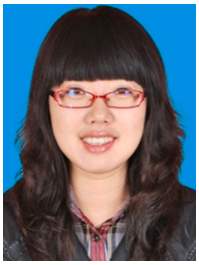

Dr. Linjuan Guo obtained her Ph.D. in Xinjiang Technical Institute of Physics & Chemistry, CAS in 2017. Then she joined the College of Physics Science and Technology at Hebei University in 2019. Her research interest mainly focuses on the design, preparation and optoelectronics applications of 2D perovskites.